



Effect of Grain Boundary and Crystallographic Orientation on the Stress Corrosion Behavior of an Al-Zn-Mg Alloy

Jianguo Tang, Yidan Zhang, Lingying Ye, Meng Qu, Jianshan Wu, Zhen Zhang, Shengdan Liu, and Yunlai Deng

(Submitted September 23, 2018; in revised form March 27, 2019; published online April 22, 2019)

The effect of grain boundary and crystallographic orientation on the stress corrosion behavior of an Al-4.5Zn-1.4Mg alloy was investigated by comparing the performance of constant load stress corrosion test (CLSCT) and tensile test of specimens parallel to the longitudinal and transverse directions of the extruded plate. The results revealed that the strength of the longitudinal and transverse specimens decreased by 9.68 and 18.13%, respectively, after 10-day CLSCT. The transverse specimens show poor resistance to stress corrosion cracking (SCC). The grain boundaries (GB) of the longitudinal section are less dense, and more of them are distributed along the extrusion direction compared with the cross section with selected areas of the same size. The SCC of all specimens starts from the side faces of the specimen, and it is dominated by intergranular cracking. But the corrosion of the transverse specimens was more serious. The cracks of all specimens tend to propagate along the GBs with misorientation of about 50°-60°, and the difference of Schmidt factor (SF) values of grains on both sides of the crack is significantly large. The crack of longitudinal specimens propagates relatively parallel to the tensile direction, while propagation of the crack in transverse specimens is more zigzag.

Keywords Al-Zn-Mg alloy, crystal orientation, high-angle grain boundaries, Schmidt factor, stress corrosion cracking

1. Introduction

Al-Zn-Mg alloys have been widely used as structural materials in high-speed railway, subway and other vehicles, due to the superior formability and strength (Ref 1-3). However, stress corrosion cracking (SCC) always causes material failure under service conditions. The factors affecting SCC have been extensively investigated to understand and reduce the SCC susceptibility. It has been found that grain boundary precipitates (GBPs) can significantly affect the SCC susceptibility of Al-Zn-Mg alloys. According to the Sun's work (Ref 4), the SCC susceptibility first decreases and then increases with the increase in the area fraction of GBPs. When the area fraction of GBPs is low, the SCC is dominated by hydrogen embrittlement, and when it is higher, anodic dissolution is the main factor. The SCC susceptibility decreases with the increase in GBPs size (Ref 4, 5), which is ascribed to the capture of hydrogen by coarse particles, especially the coarse $MgZn_2$ particles, to reduce the concentration of hydrogen which causes hydrogen embrittlement (Ref 4, 6). And the discontinuous distributed GBPs can inhibit the corrosion cavities from connecting into a continuous crack (Ref 7). Cheng Cao et al. (Ref 8) reported that adding copper to Al-

5.2Mg-2.0Zn alloy can efficiently enhance the intergranular cracking resistance. Several works (Ref 7, 9-11) reported that the copper in the GBPs of the Al-Zn-Mg alloy can decrease the potential difference between precipitates and adjacent matrix and improve the SCC resistance. In the slowly quenched specimens, because of the increase in Zn and Mg content in the GBPs, the positive effect of Cu could not exceed the negative effect of Zn and Mg and the GBPs became more active and lead to low resistance (Ref 12). Some researchers (Ref 13, 14) ascribed the embrittlement and the decrease in the strength of grain boundaries to the segregation of Mg atoms at grain boundaries. The diffusion of H atoms at grain boundaries where Mg is prone to segregate, and its interaction with the segregated Mg atoms accelerate the process of hydrogen-induced embrittlement. Additionally, a number of conventional methods of surface engineering have been applied to obtain functional coating to improve the mechanical and corrosion properties (Ref 15-17). And the profitable method for improvement of physicochemical properties of Al-Zn-Mg alloys may be the two-stage artificial aging process during surface modification (Ref 17).

Many studies about the effect of grain size and grain boundary on corrosion were carried out. Some researchers (Ref 18, 19) revealed the relationship between corrosion rate and grain size in high-purity aluminum, i.e., the corrosion rate tended to decrease with decreasing grain size. Corrosion takes place at the grain boundaries due to the formation of micro-cells between the PFZ and the grain boundary precipitates or the matrix (Ref 20). Meng et al. (Ref 21) reported that the low-angle grain boundaries show good resistance to intergranular corrosion. There were some differences of corrosion resistance between the recrystallized grains and fibrous grains in the deformed microstructure. Sinyavskii (Ref 22) proposed that corrosion active areas tended to be formed at the high-angle grain boundaries (HAGBs) of recrystallized grains and caused the intergranular corrosion at certain stage of recrystallization, i.e., the cracks tended to propagate along the HAGBs of

Jianguo Tang and Yunlai Deng, School of Materials Science and Engineering, Central South University, Changsha 410083, China; and Research Institute of Light Alloy, Central South University, Changsha 410083, China; and Yidan Zhang, Lingying Ye, Meng Qu, Jianshan Wu, Zhen Zhang, and Shengdan Liu, School of Materials Science and Engineering, Central South University, Changsha 410083, China. Contact e-mail: lingyingye@csu.edu.cn.

recrystallized grains (Ref 23). Therefore, the recrystallized grains are more susceptible to corrosion than the fibrous grains (Ref 24). Some investigators tried to improve the corrosion resistance of aluminum alloys by adding trace elements and modifying the heat treatment to inhibit recrystallization during hot deformation and heat treatment (Ref 25-28).

Many researchers have studied the SCC susceptibility of alloys in terms of alloy composition and heat treatment (Ref 29-

31), which always need different samples with different compositions and/or subjected to different thermo-mechanical treatment. In the present paper, the effect of grain boundary character on the stress corrosion behavior of Al-4.5Zn-1.4Mg alloy was studied by analyzing the difference of grain boundary character in different side faces of an extruded plate and comparing the performance of constant load stress corrosion test (CLSCT) and tensile test of longitudinal and transverse

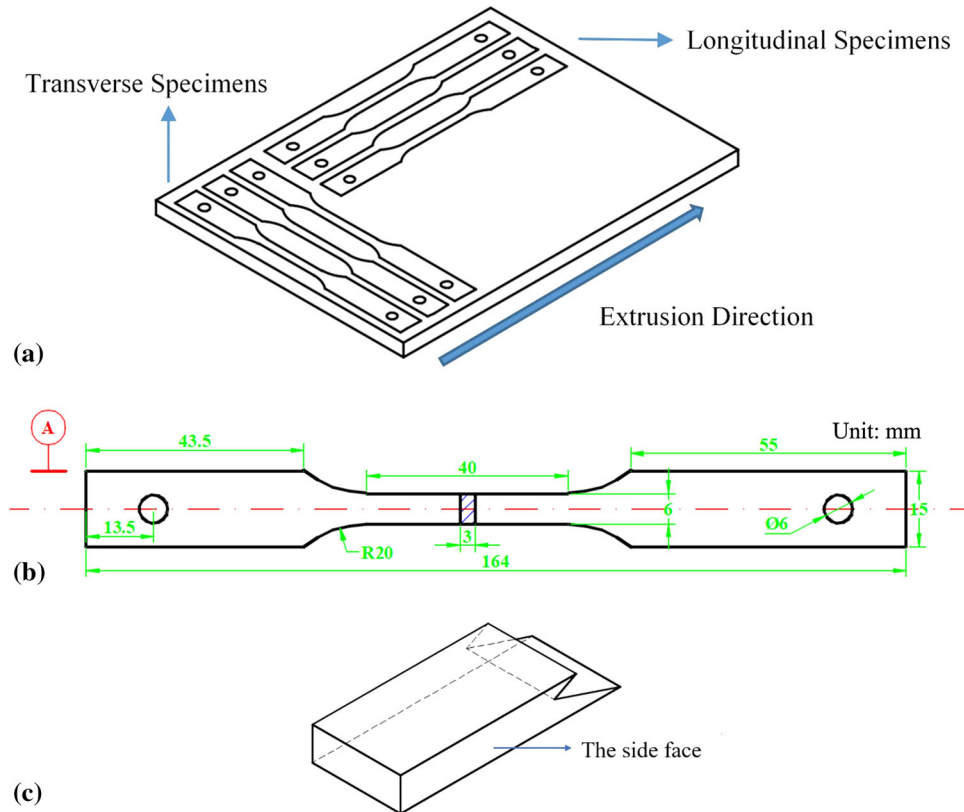


Fig. 1 Schematic diagram for specimens and fracture: (a) specimens cutting direction; (b) specimen size specifications; (c) fracture mode



Fig. 2 Three-dimensional views of the microstructures of the alloy

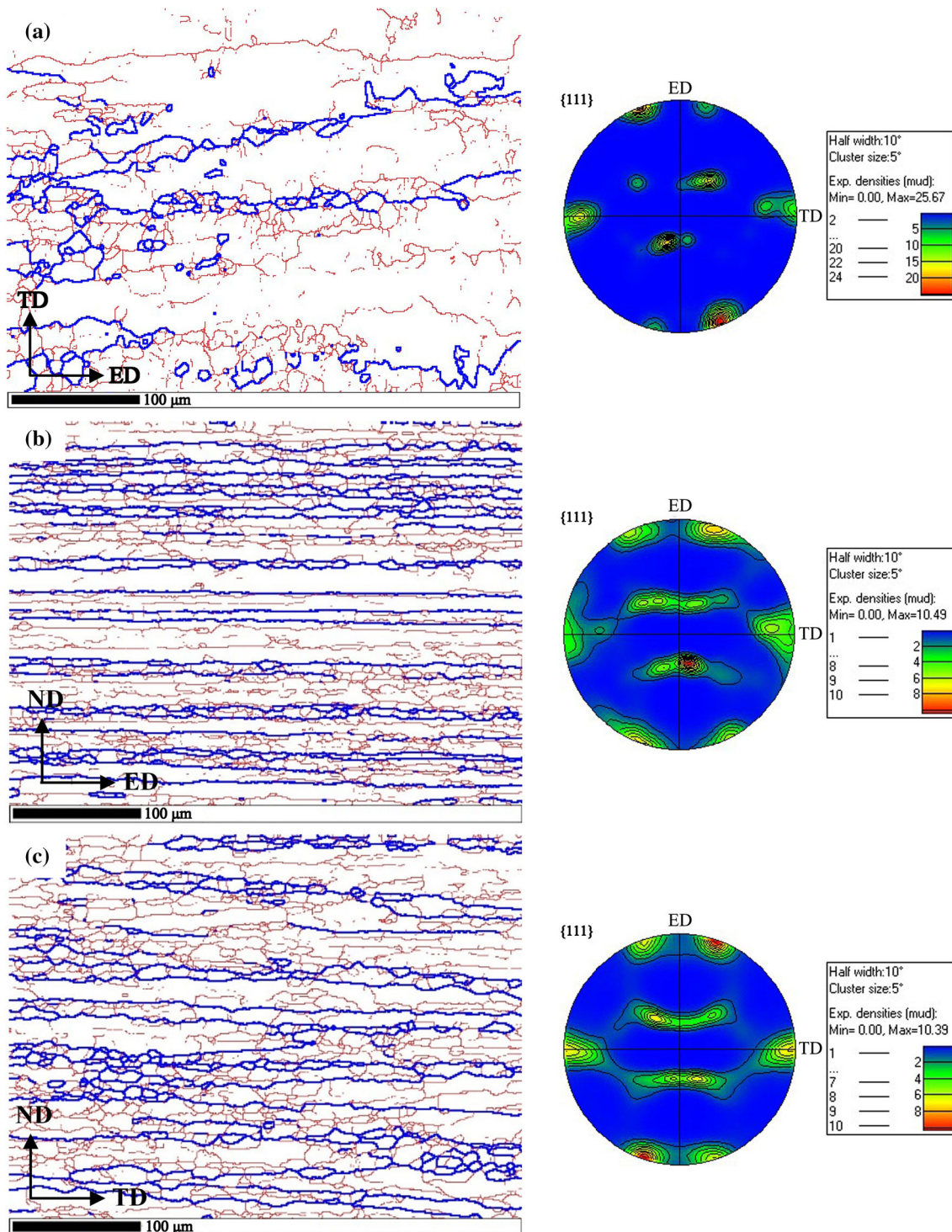


Fig. 3 EBSD misorientation maps and pole figures: (a) top surface layer; (b) longitudinal section and (c) cross section

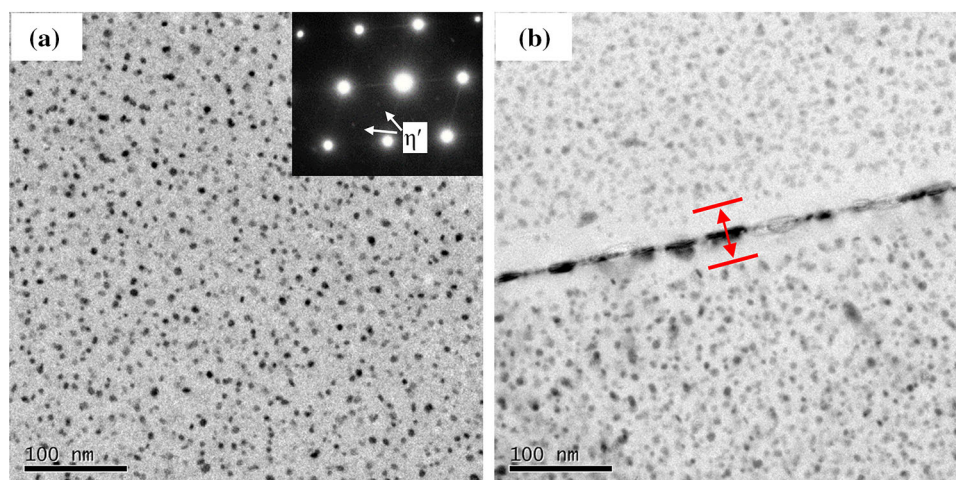
specimens. Furthermore, stress is another reason that should not be ignored. In this paper, the analysis of Schmidt factor (SF) is used to resolve maximum shear stress of grains on specific slip system according to the external loading to account for possible plastic deformation before cracking. This investigation presents the effect of different grain boundary character and shear stress acting on crystallographic slip system correlated with SF between longitudinal and transverse direction on SCC and crack propagation.

2. Experimental

The material used in this study is a commercial Al-Zn-Mg alloy in T5 temper, provided by Research Institute of Light Alloy of Central South University, and then the plate was artificially aged at 120 °C for 24 h (peak-aged). The chemical composition is given in weight percent: 4.51 Zn, 1.43 Mg, 0.01 Cu, 0.14 Fe, 0.14 Si, 0.31 Mn, 0.23 Cr, 0.07 Ti, 0.13 Zr.

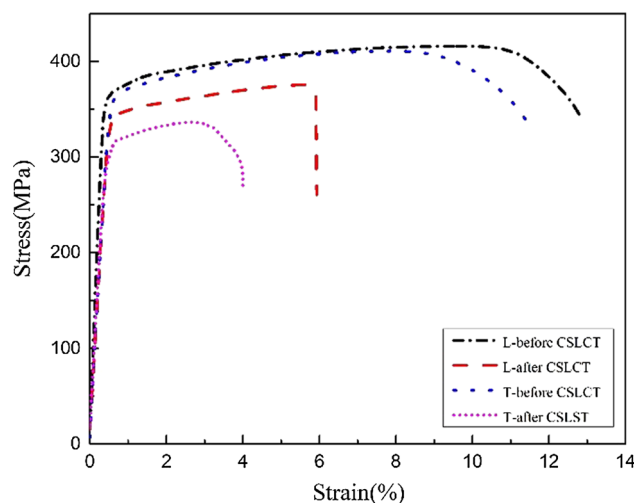
Table 1 EBSD statistical data

	Top surface layer	Longitudinal section	Cross section
Frequency of low-angle grain boundaries, %	60.75%	45.12%	47.06%
Frequency of high-angle grain boundaries, %	14.89%	30.08%	30.44%
Average grain size, μm	14.31	18.89	14.32
Standard deviation of grain size, μm	32.78	24.65	22.51
Number of grains	116	159	233
Aspect ratio	1.797	8.256	3.895
Brass texture	81.5%	58.3%	55.8%
Average grain size, standard deviation of grain size, number of grains and aspect ratio account for the grains defined by HAGBs.			

**Fig. 4** TEM images showing the precipitates in the (a) matrix and (b) grain boundary

2.1 Corrosion Tests

The CLSCT was used to evaluate the SCC susceptibility of the alloys. Specimens with their tensile axes parallel or perpendicular to the extrusion direction of the extruded plate for CLSCT are schematically shown in Fig. 1(a). They were named as longitudinal specimens (L) and transverse specimens (T). The schematic diagram of sample size is shown in Fig. 1(b). The thickness of the sample is 3 mm, and the parallel length is 40 mm. The specimens were divided into two groups. One group of specimens were directly tested by conventional room temperature tensile test. The specimens of the other group were completely immersed in the corrosive solution (a mixture of 30 g NaCl, 10 ml H₂O₂ and 1 L deionized water) with a constant unidirectional loading of 225 MPa for 10 days and then the conventional room temperature tensile test was carried out to evaluate the loss of mechanical properties with 10 days CLSCT, which is used to characterize the SCC resistance. To ensure the reliability of the results, the transverse and longitudinal samples were tested under the same experimental conditions, and there was no visible extension or cross sections reduction after 10-day CLSCT. And six samples (three transverse samples and three longitudinal samples) should be tested for each set of experiments.

**Fig. 5** Tensile stress–strain curves of longitudinal and transverse specimens without and with 10-day CLSCT

2.2 Microstructure Examination

The fractography of the tensile test specimens without and with CLSCT was examined by scanning electron microscopy

(SEM). The side face of the fracture (as shown in Fig. 1c) and the granular microstructure of the alloy were revealed by optical microscopy (OM). The grain boundaries of the top surface layer, longitudinal section and cross section were investigated by electron backscattered diffraction (EBSD) system mounted on Zeiss EVO MA10. The crystallographic orientation and SF of the grains on both sides of the stress corrosion crack and corresponding grain boundary character distribution were also investigated by EBSD. Specimens for EBSD investigation were electropolished for 10 s in a solution of 10 vol.% perchloric acid and 90 vol.% C₂H₅OH at room temperature. The test results were processed by channel 5. The distribution and morphology of precipitates in both the grain boundary and the matrix were investigated by transmission electron microscopy (TEM, TECNAI G2 F20). Specimens for TEM were cut in the form of thin slice. Disks of 3 mm in diameter were then punched from the slices and finally thinned by a twin-jet polishing technique in a solution (30 vol.% nitric and 70 vol.% methanol) at -20 °C.

3. Results

3.1 The Microstructure of the Extruded Aluminum Alloy

3.1.1 Optical Microscopy Results. Three-dimensional views of the granular microstructures of the investigated Al-Zn-Mg alloy revealed by optical microscopy are shown in Fig. 2. The top surface layer (ED-TD) of the plate showed heterogeneous distribution of coarse elongated grains. The aspect ratio of grains of longitudinal section is much larger than that of cross section.

3.1.2 EBSD Results. The EBSD misorientation maps and pole figures of the top surface layer, longitudinal and cross sections of the extruded plate are shown in Fig. 3, and high-angle grain boundaries (HAGBs), the misorientation angle of which is above 15°, and low-angle grain boundaries (LAGBs) are depicted as thick blue lines and thin red lines, respectively. The statistical data are listed in Table 1. For the top surface layer (ED-TD) of the plate, the grain size is very heterogeneous, and most of the grain boundaries are distributed along the extrusion direction. Compared with the other two sides, its

LAGBs and brass texture take a large proportion. No significant difference is presented in the fraction of HAGBs, LAGBs and brass texture between longitudinal section and cross section. However, in the selected area of same size, the number of grains in the longitudinal and cross section is 159 and 233, respectively, i.e., the average grain size is 18.89 and 14.32 μm,

Table 2 Tensile properties of longitudinal and transverse specimens without and with 10-day CLSCT

	Ultimate tensile strength, MPa	Yield strength, MPa	Elongation rate, %
Longitudinal specimens			
Without CLSCT	415.94 ± 1.12	371.84 ± 2.54	12.8
With CLSCT	375.66 ± 5.98	347.08 ± 3.65	6.14
Loss ratio	9.68%	6.66%	52.34
Transverse specimens			
Without CLSCT	410.83 ± 2.71	369.88 ± 3.52	11.4
With CLSCT	336.36 ± 5.08	326.39 ± 1.22	4.02
Loss ratio	18.13%	11.76%	64.73

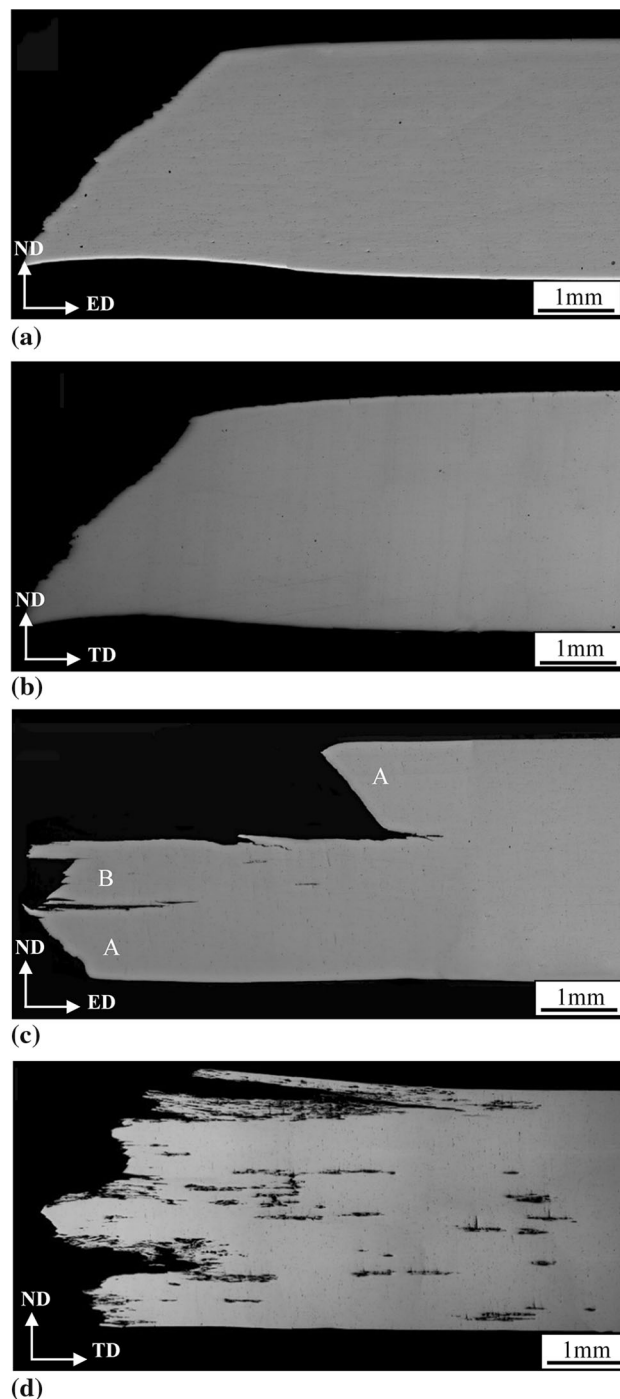


Fig. 6 Optical microscopy images of the side face of the fracture: (a) longitudinal specimen without CLSCT; (b) transverse specimen without CLSCT; (c) longitudinal specimen with CLSCT and (d) transverse specimen with CLSCT

respectively, and the aspect ratio of grains within longitudinal section (8.256) is much larger than that within the cross section (3.895). The above results mean that the GBs of the longitudinal section are less dense and more of them are aligned along the extrusion direction compared with that of the cross section.

3.1.3 TEM Observations. Figure 4 displays the distribution of precipitates in the matrix and grain boundary of the investigated alloy by TEM observations. A large number of fine and dispersed precipitates are distributed in the matrix (as shown in Fig. 4a). According to the morphology and $\langle 110 \rangle_{\text{Al}}$ select area diffraction pattern, the precipitates are particles of η' phase. The grain boundary is dominated by the continuously distributed and coarse phases. It is generally accepted that the phases are η phases (Ref 4, 24, 27). What is more, precipitate-free zone (PFZ) is observed along grain boundary, and the measured width of PFZ is about 54.45 nm.

3.2 SCC Susceptibility of the Alloys

The stress-strain curves of tensile test of both longitudinal and transverse specimens without and with 10-day CLSCT are shown in Fig. 5, and corresponding strength, elongation rates and the rate of loss after CLSCT are listed in Table 2. It is clearly demonstrated that there is no significant difference in the conventional tensile properties between two kinds of

specimens, but the transverse specimens show a higher loss rate in strength and elongation rate with 10-day CLSCT. For the longitudinal specimens after 10-day CLSCT, the ultimate tensile strength and the yield strength are 375.66 and 347.08 MPa, respectively, and the elongation rate is 6.14%. Compared with the conventional tensile properties at room temperature, the loss rate is 9.68, 6.66 and 52.34%, respectively. For the transverse specimens, the ultimate tensile strength and the yield strength are 336.36 and 326.39 MPa, respectively, and the elongation rate is 4.02%, and the corresponding losing rate is 18.13, 11.76 and 64.73%, respectively. The results indicate that the loss of elongation rate is the most serious one for all specimens, and the transverse specimens show a higher loss rate of tensile properties, which indicates that the SCC susceptibility of transverse specimens is higher than that of the longitudinal specimens.

3.3 Macroscopic Characteristic of Fracture

Optical microscopy images of the side face near the fracture of tensile test without and with CLSCT are shown in Fig. 6. Figure 6(a) and (b) shows typical tensile fractures on longitudinal and transverse specimens, respectively. Something like necking was found in those tensile tests at room temperature, and the angle between the fracture surface and tensile direction

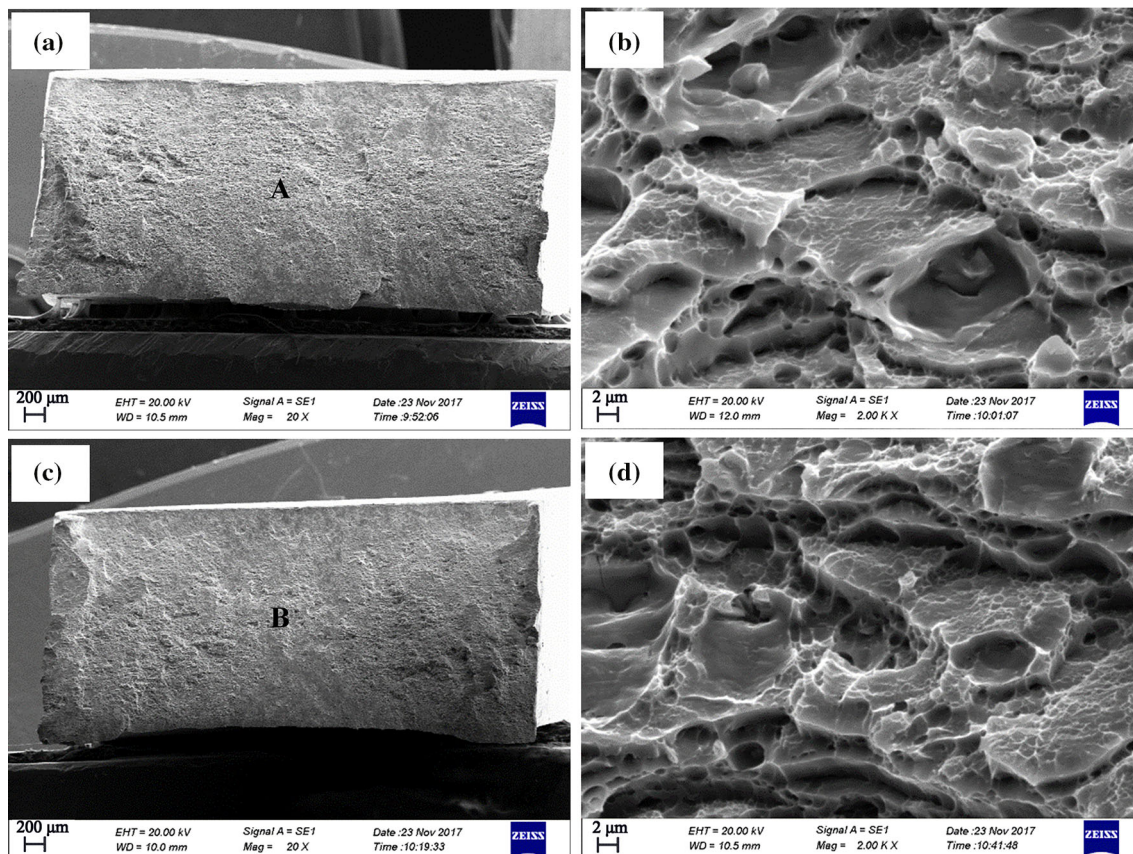


Fig. 7 SEM images of the fractography after tensile test: (a) macro-morphology of longitudinal specimen; (b) the high-magnification images of area A; (c) macro-morphology of transverse specimen and (d) the high-magnification images of area B

is about 45° . But that of the longitudinal specimens (Fig. 6c) with 10-day CLSCT shows two distinctive parts. Several small cracks propagated along the tensile direction were found in the middle part which was denoted as B in Fig. 6(c), and area near to the top surface of the specimen shows the fracture characteristic same to that found in Fig. 6(a) and (b). For transverse specimens, as shown in Fig. 6(d), the specimen shows many small cracks that were seriously corroded with 10-day CLSCT. Exfoliation corrosion was found on the surface layer near the fracture. There are only few sections of the fracture propagated with an angle of 45° to the tensile direction.

3.4 The Fractography of Specimens After Tensile Test and CLSCT

The fractography of both longitudinal and transverse specimens without CLSCT is shown in Fig. 7. There is no significant difference between longitudinal and transverse specimens. The fractography shows ductile rupture with characteristic dimples observed in the high-magnification images.

Figure 8 shows the SEM images of the fractography of the longitudinal specimen with CLSCT. It is obvious that the fracture includes ductile rupture (A) and SCC (B and C) from the low-magnification image of overall fracture surface (shown in Fig. 8a). Area A is close to the surface layer, and the high-

magnification image is shown in Fig. 8(b). Noticeable dimples are found, which indicates that area A should be the final ductile rupture zone in the tensile test. The high-magnification image of area B is shown in Fig. 8(c). The intergranular cracking feature is observed and runs through the whole fracture along the width direction of the fracture. The high-magnification image of area C (shown in Fig. 8d) clearly shows the evidence that the SCC starts from the side of the fracture.

Figure 9 shows the SEM images of the fractography of transverse specimen with CLSCT. A large number of stress corrosion cracks propagating from the side face to the center can be clearly found and shown in area B, and the propagation in the middle part is the deepest. Similarly, many dimples are found in the high-magnification image of area A (shown in Fig. 9b), while the intergranular cracking feature is observed in the high-magnification image of area B (shown in Fig. 9c).

From the appearance of the fractography after tensile test at room temperature, there is no obvious difference between longitudinal specimens and transverse specimens. The fractography of specimens with CLSCT shows that the SCC starts from the side face of the fracture, and it is characterized by the intergranular cracking. Compared with the longitudinal specimens, the transverse ones show a larger corrosion area and more serious corrosion.

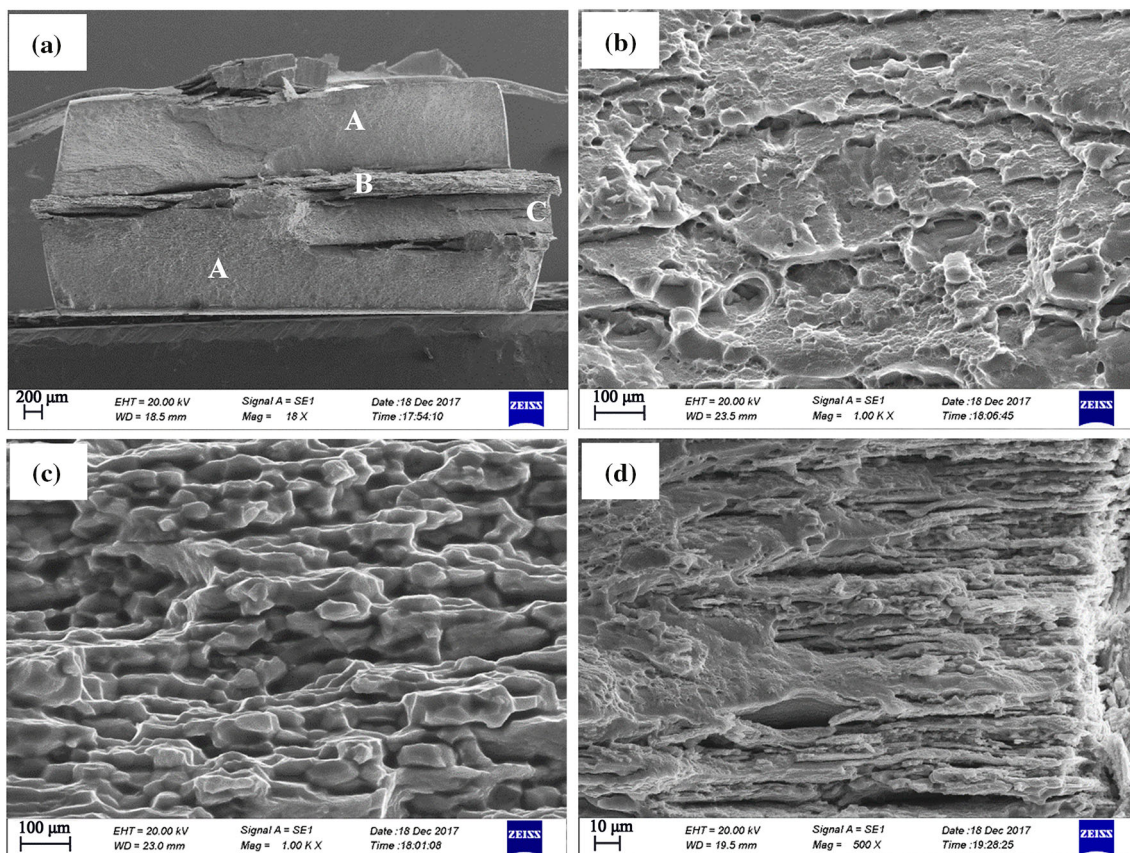


Fig. 8 SEM images of the fractography after CLSCT of longitudinal specimen: (a) macro-morphology; (b), (c) and (d) are high-magnification images of areas A, B and C, respectively

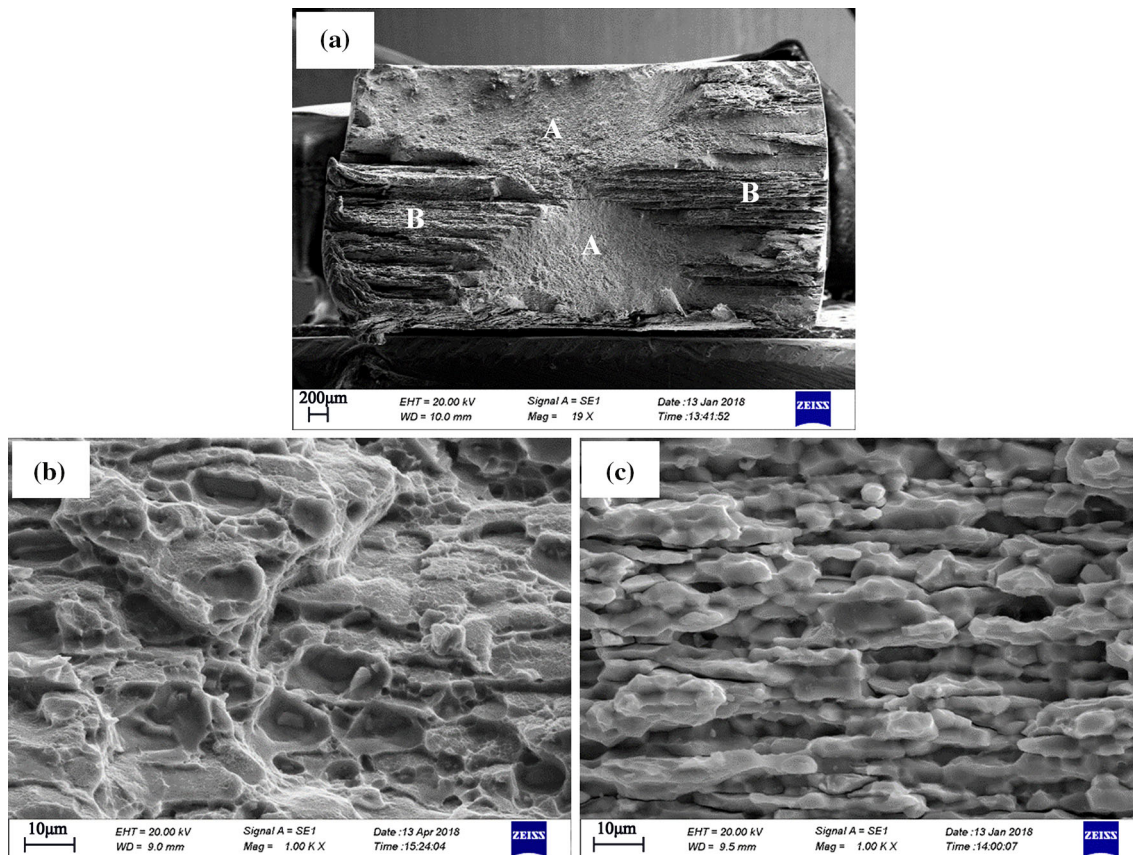


Fig. 9 SEM images of the fractography after CLSCT of transverse specimen: (a) macro-morphology; (b) and (c) are high-magnification images of areas A and B, respectively

3.5 EBSD Results of Areas Near the Stress Corrosion Crack

Figure 10 shows EBSD maps of the stress corrosion crack found on the side face of the fracture of longitudinal specimen after CLSCT. The cracks are marked by the thick and black lines in Fig. 10(c), (d) and (e). As can be seen from Fig. 10(a) and (b), the cracks are small and discontinuous, which is typical intergranular cracking. The misorientation angles between grains on both sides of the crack shown in Fig. 10(c) are calculated. The result indicates that most segments of the crack propagated along the HAGBs, except for the segments between grains 25 and 26, grains 29 and 30. As shown in Fig. 11, the misorientation angles of more than 95% pair of grains on both sides of the crack are larger than 10° and dominated with a fraction of 36% by angles between 50° and 60° . So the crack tends to propagate along the GBs with misorientation of about 50° - 60° . Figure 10(d) shows the Schmidt factor map. When calculating the SF by channel 5, we set the slip system as $\{111\} \langle 1-10 \rangle$ and the stress direction parallel to the loading direction. The lighter the color, the higher the SF value. The distribution of SF values is illustrated in Fig. 12; it changes significantly at 0.4. In this selected area, there are 65% grains whose SF values are greater than 0.4, which are the grains with light color shown in Fig. 10(d). And the SF values of 84.21%

grains on both sides of the crack are above 0.4. As shown in Fig. 10(e), the color of the grains of 18, 20, 21 and 23 on one side of crack is lighter, and their SF values are 0.47, 0.48, 0.5 and 0.46, while the SF values of 19, 22 and 24 on the other side are 0.39, 0.41 and 0.42, respectively. So the crack tends to propagate along the GBs with significant difference of SF values between grains on both sides of the crack.

EBSD maps and distribution of misorientation of the grains on both sides of the stress corrosion crack of transverse specimen after CLSCT are represented in Fig. 13 and 14, respectively. The cracks are marked by the thick and black lines in Fig. 13(c), (d), (e) and (f). Similar to the longitudinal specimen, the crack is featured by tiny and intermittent segments (Fig. 13a and b) and tends to propagate along the GBs with misorientation of 50° - 60° between neighboring grains (Fig. 14). But the propagating path of the crack is more zigzag than that of longitudinal specimen and tends to the direction of maximum shear stress, i.e., the crack propagates macroscopically with angle of about 45° to the tensile direction. The distribution of SF values provided in Fig. 15 clearly demonstrated that the distribution of SF values of the grains on both sides of the crack has a significant difference from that of the grains of entire selected area. Figure 13(e) is the enlarged

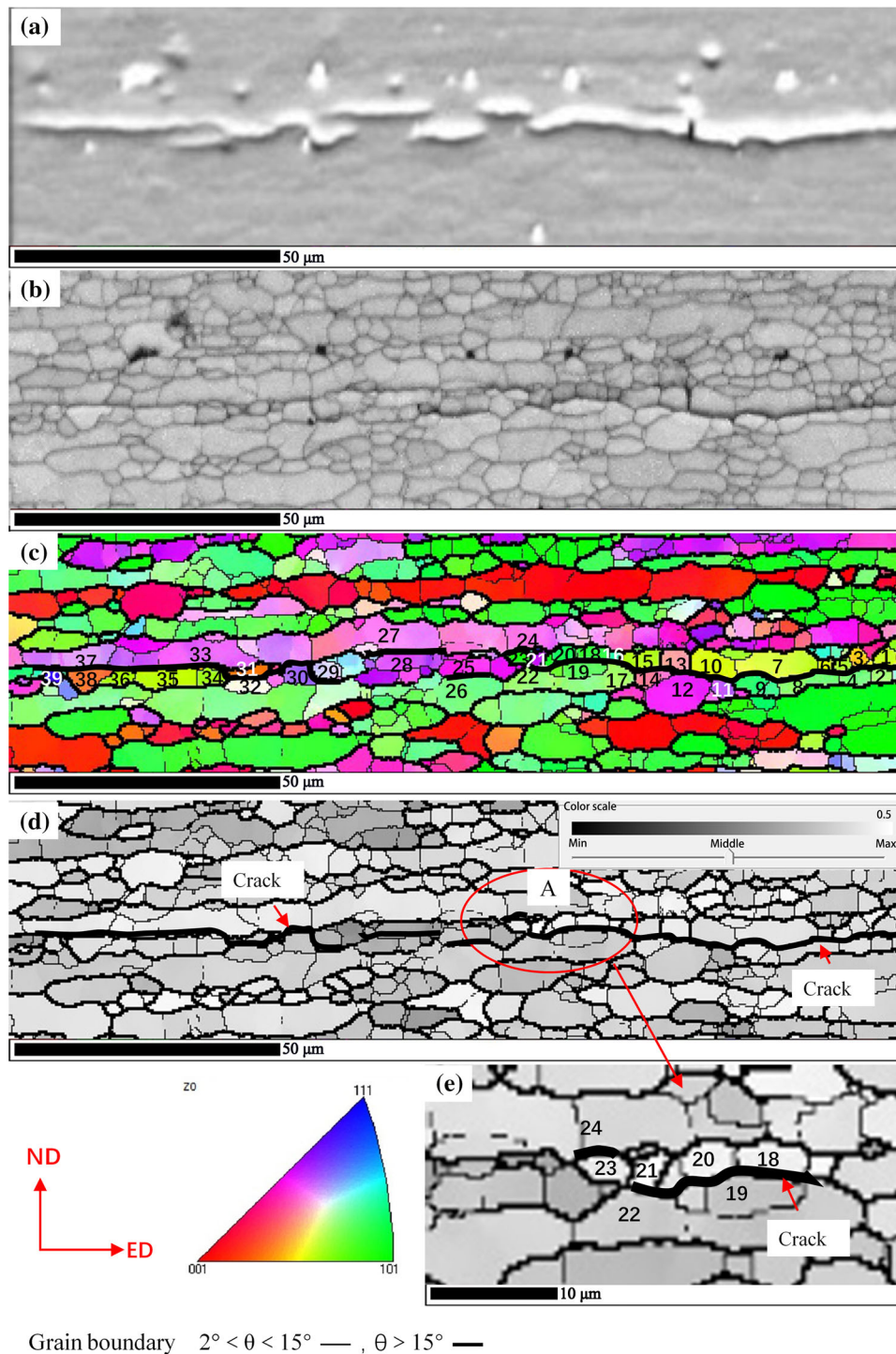


Fig. 10 EBSD maps for longitudinal specimen: (a) SEM image; (b) band contrast map; (c) IPF map; (d) Schmidt factor map and (e) is the high-magnification image of area A in (d)

figure of area A. It can be seen the grains (3, 7, 9 and 11) on one side of the crack are darker in color and the average SF value is 0.38, while the others (5, 6, 8, 10 and 12) are lighter and the average SF value is 0.46. Figure 13(f) is the enlarged

figure of area B. The SF values of the grains (39, 41, 43, 45 and 47) on one side of crack are 0.48, 0.4, 0.41, 0.45 and 0.44, respectively. And the corresponding SF values of the grains (40, 42, 44 and 46) on the other side are 0.34, 0.32, 0.34 and

0.35, respectively. So the crack tends to propagate along the GBs between grains with significant difference of SF values, which is consistent with that of longitudinal specimen. As the external loading direction for the longitudinal and transverse specimens is different, i.e., ED for longitudinal specimen and TD for transverse specimen, the SF values of longitudinal (Fig. 12a) and transverse specimen (Fig. 15a) differ.

4. Discussion

There are two main theories about the SCC of aluminum alloys, hydrogen embrittlement (Ref 32-34) and anodic dissolution (Ref 35). The theory of hydrogen embrittlement holds that under the effect of tensile stress, the hydrogen produced in the corrosion environment migrates to the GBs by dislocation

and accumulates near the precipitates to reduce the bonding strength of GBs and make them brittle. Anodic dissolution model argues that there is potential difference between GBPs and adjacent areas, resulting in GBPs to be dissolved as an anode. In addition, the continuous distribution of GBPs is easy to form corrosive channels, reducing the mechanical properties and leading to fracture.

The experimental results prove that the initiation and propagation of SCC are systematically related to the grain boundary. Fractographic investigations (Fig. 8 and 9) show that the SCC starts from the side face and propagates to the center. The possible reason why no SCC initiation was observed from the ND surface is that there were few HAGBs on ND surface. The SCC fractography shows the intergranular characteristic, which conforms to the anodic dissolution theory (Ref 35, 36). Discontinuous cracks were found in the side face near the fracture, which is in line with the theory of hydrogen embrittlement (Ref 7, 32). Under the effects of the load, the grain boundaries are torn and corroded by corrosive solution, and then local anodic dissolution occurs. It can be seen from the TEM results (Fig. 4b) that the distribution of GBPs is relatively continuous, so it is easy to form a corrosion channel and accelerates the corrosion rate (Ref 7). When the hydrogen in the corrosive environment scrapes up to a certain concentration, it accumulates on the grain boundaries or crack tips, causing stress concentration and making GBs brittle. Hydrogen atoms are produced by the reduction of H^+ ions, which is a cathodic reaction at metal surface (Ref 37, 38). The corroded grain boundaries will provide a channel for the expansion of hydrogen and corrosive solution, which in turn causes further corrosion. The corrosion procedure greatly reduces the effective area to bear the load and results in the loss of mechanical properties.

For the longitudinal specimens, the number of grain boundaries within the side face is small, and the HAGBs are mostly distributed along the extrusion direction (Fig. 3b). At the effect of the force, the SCC occurs on the two side faces of the specimen and propagates to the center along the width direction, until it penetrates the entire specimen (Fig. 8). And

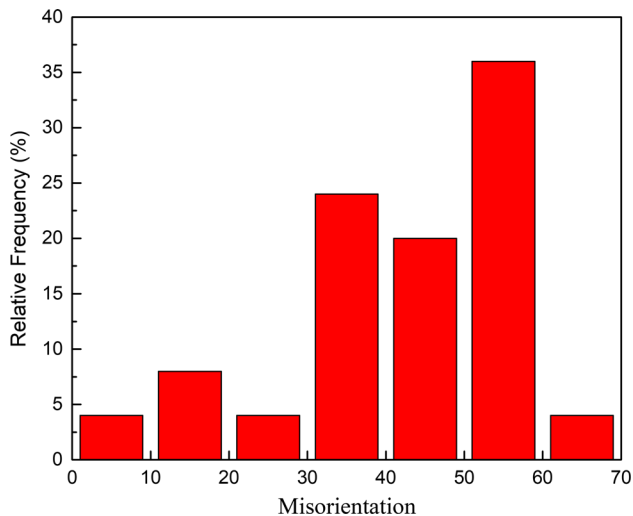


Fig. 11 Distribution of misorientation angles between the grains on both sides of the crack of the longitudinal specimen

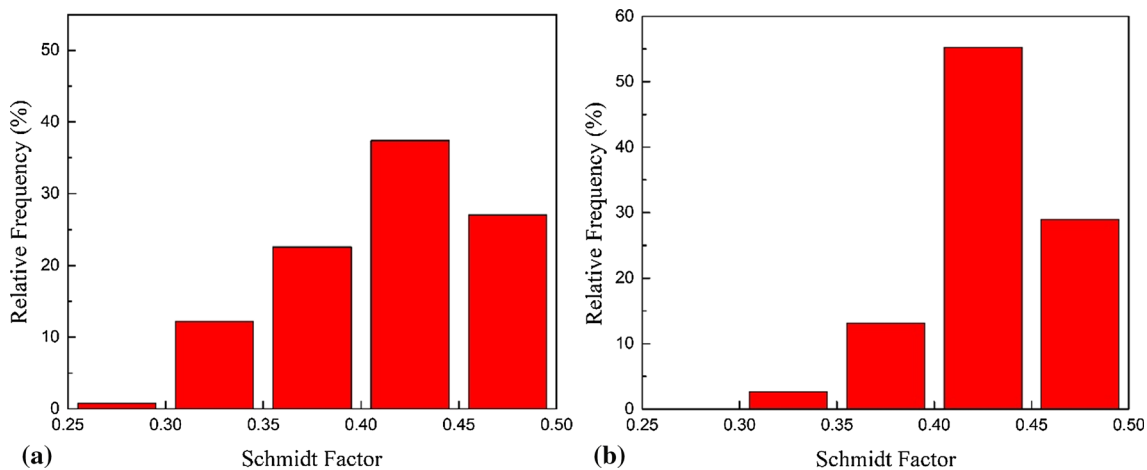


Fig. 12 The distribution of the Schmidt factors of (a) the grains of entire selected area shown in Fig. 10(d) and (b) the grains on both sides of the crack for longitudinal specimen

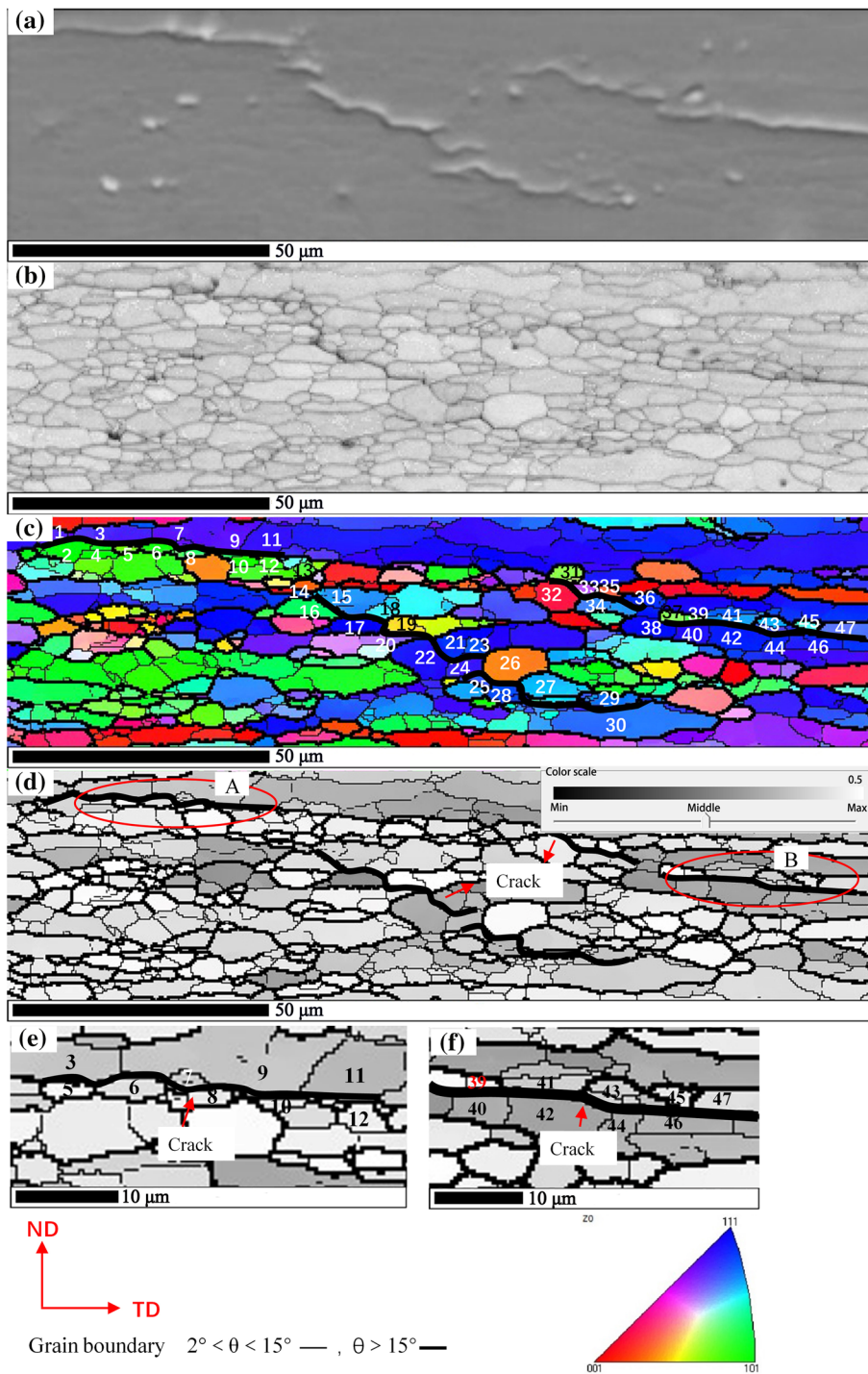


Fig. 13 EBSD maps for transverse specimen: (a) SEM image; (b) band contrast map; (c) IPF map; (d) Schmidt factor map; (e) and (f) are the high-magnification images of areas A and B in (d), respectively

then, the corrosive agents invade adjacent areas of the corroded area (Fig. 8d), in which SCC occurs and begins to propagate again. However, for the transverse specimens, more HAGBs (Fig. 3c) provide more sites for the initiation of SCC. The SEM images of the fracture surface (Fig. 9) present that stress corrosion cracks initiate from several positions on the side face

and propagate to the center. The transverse specimens are seriously corroded (Fig. 6d), and the corrosion area is larger than that of the longitudinal specimens. So the loss of strength and the loss of elongation rate of transverse specimens are greater than those of longitudinal specimen. The grains are elongated along the extrusion direction, and more of grain

boundaries are also distributed along the extrusion direction. For the longitudinal specimen, the loading direction is parallel to the extrusion direction, and the grains deform along the brittle grain boundary during loading, and therefore, the fracture is characterized as a ladder, while the transverse specimen has a relatively flat fracture (Fig. 6d).

The stress corrosion cracks are small and discontinuous, which is in good agreement with the results reported by Ref 32. The cracks tend to propagate along the GBs with misorientation of 50°-60° between neighboring grains, as the high energy GBs are easy to be corroded. Most HAGBs of longitudinal specimens are aligned along the extrusion direction, so the crack propagates parallel to the tensile direction. For transverse specimens, the high density of HAGBs makes the cracks ramified. The crack propagation is more zigzag and tends to propagate along the direction of maximum shear stress.

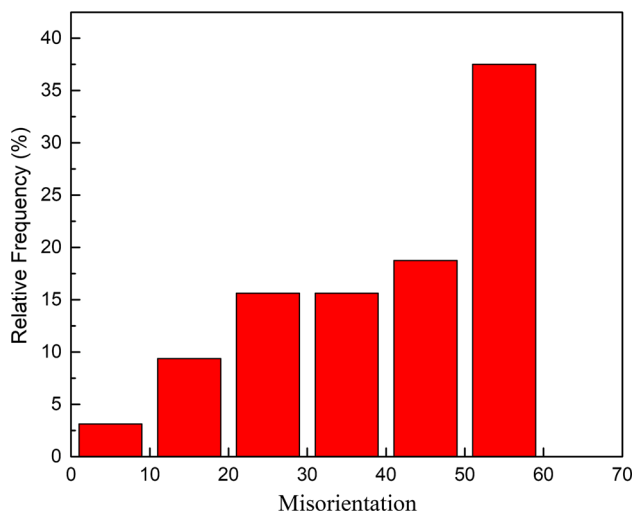


Fig. 14 Distribution of misorientation angles between the grains on both sides of the crack of the transverse specimen

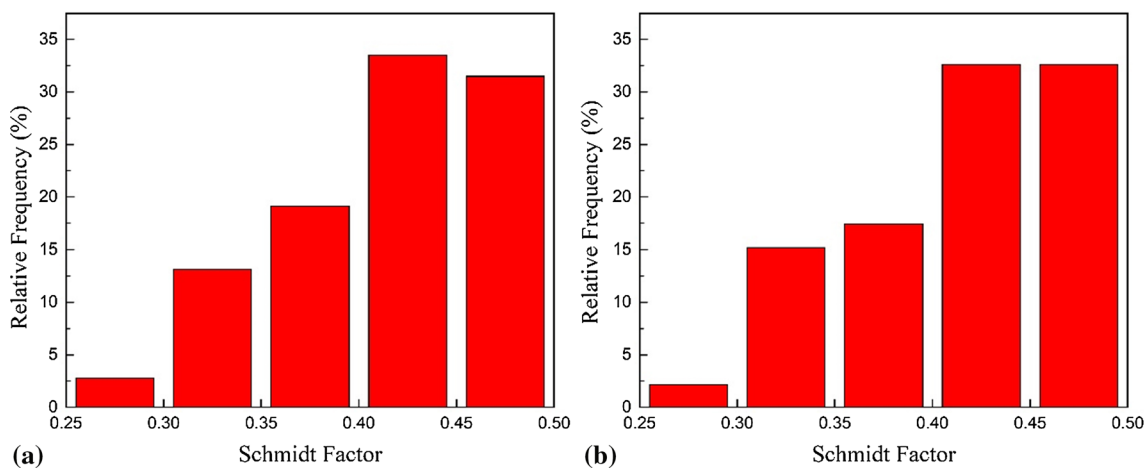


Fig. 15 The distribution of the Schmidt factors of (a) the grains of entire selected area shown in Fig. 13(d) and (b) the grains on both sides of the crack for transverse specimen

The larger the SF value, the greater the shear stress acting on the slip system, and therefore, the grains are easy to deform. The GBs whose both sides grains have a significant difference in the values of SF become unstable, easy to be corroded and then crack.

5. Conclusions

To summarize, this paper shows the following:

- (1) After loading for 10-day CLSCT, the loss of ultimate tensile strength for transverse specimens is 18.13%, larger than that of longitudinal specimens (9.68%), and the elongation loss (64.73%) is much higher than that of longitudinal specimens (52.34%). The elongation loss is the most serious one for all specimens, and the transverse specimens show a higher loss rate of tensile properties and SCC susceptibility than longitudinal specimens.
- (2) The stress corrosion cracking starts from the side face and propagates to the center, and the corroded area is featured by intergranular cracking. For longitudinal specimens, the grain boundaries of the side face are less dense, and more of them are distributed along the extrusion direction. The intergranular cracking propagates on the both sides of the specimen and runs through the whole fracture along the width direction. The fracture is characterized as a ladder. However, for the transverse specimens, more grain boundaries provide more sites for the initiation and more channels for the propagation, and the corrosion area is larger than that of the longitudinal specimens.
- (3) The stress corrosion cracks are small, discontinuous, and tend to propagate the GBs with misorientation of 50°-60° between adjacent grains. The SF values on both sides of the crack are always significantly different. The crack of longitudinal specimens propagates relatively

parallel to the tensile direction, while the crack propagation of transverse specimens is more zigzag and tends to the direction of maximum shear stress.

Acknowledgments

This present work was supported by National Natural Science Foundation (Project No. 51474240) and Provincial Science and Technology Major Project of Hunan province (Project No. 2016KG1004), which are greatly acknowledged by the authors.

References

1. A. Heinz, A. Haszler, C. Keidel, S. Moldenhauer, R. Benedictus, and W.S. Miller, Recent Development in Aluminium Alloys for Aerospace Applications, *Mater. Sci. Eng. A*, 2000, **280**, p 102–107
2. W.S. Miller, L. Zhuang, J. Bottema, A.J. Wittebrood, P. De Smet, A. Haszler, and A. Vierregge, Recent Development in Aluminium Alloys for the Automotive Industry, *Mater. Sci. Eng. A*, 2000, **280**, p 37–49
3. J. Hirsch and T. Al-Samman, Superior Light Metals by Texture Engineering: Optimized Aluminum and Magnesium Alloys for Automotive Applications, *Acta Mater.*, 2013, **61**, p 818–843
4. X.Y. Sun, B. Zhang, H.Q. Lin, Y. Zhou, L. Sun, J.Q. Wang, E.H. Han, and W. Ke, Correlations Between Stress Corrosion Cracking Susceptibility and Grain Boundary Microstructures for an Al-Zn-Mg Alloy, *Corros. Sci.*, 2013, **77**, p 103–112
5. Y.P. Xiao, Q.L. Pan, W.B. Li, X.Y. Liu, and Y.B. He, Influence of Retrogression and Re-aging Treatment on Corrosion Behaviour of an Al-Zn-Mg-Cu Alloy, *Mater. Des.*, 2011, **32**, p 2149–2156
6. T.C. Tsai and T.H. Chuang, Role of Grain Size on the Stress Aluminum Alloys, *Mater. Sci. Eng. A*, 1996, **225**, p 135–144
7. J. Chen, X. Zhang, L. Zou, Y. Yu, and Q. Li, Effect of Precipitate State on the Stress Corrosion Behavior of 7050 Aluminum Alloy, *Mater. Charact.*, 2016, **114**, p 1–8
8. C. Cao, D. Zhang, X. Wang, Q. Ma, L. Zhuang, and J. Zhang, Effects of Cu Addition on the Precipitation Hardening Response and Intergranular Corrosion of Al-5.2Mg-2.0Zn (wt%) Alloy, *Mater. Charact.*, 2016, **122**, p 177–182
9. S.P. Knight, N. Birbilis, B.C. Muddle, A.R. Trueman, and S.P. Lynch, Correlations Between Intergranular Stress Corrosion Cracking, Grain-Boundary Microchemistry, and Grain-Boundary Electrochemistry for Al-Zn-Mg-Cu Alloys, *Corros. Sci.*, 2010, **52**, p 4073–4080
10. G. Peng, K. Chen, S. Chen, and H. Fang, Influence of Repetitious-RRA Treatment on the Strength and SCC Resistance of Al-Zn-Mg-Cu Alloy, *Mater. Sci. Eng. A*, 2011, **528**, p 4014–4018
11. T. Ramgopal, P.I. Gouma, and G.S. Frankel, Role of Grain-Boundary Precipitates and Solute-Depleted Zone on the Intergranular Corrosion of Aluminum Alloy 7150, *Corrosion*, 2012, **58**, p 687–697
12. S.D. Liu, B. Chen, C.B. Li, Y. Dai, Y.L. Deng, and X.M. Zhang, Mechanism of Low Exfoliation Corrosion Resistance Due to Slow Quenching in High Strength Aluminium Alloy, *Corros. Sci.*, 2015, **91**, p 203–212
13. R.G. Song, W. Dietzel, B.J. Zhang, W.J. Liu, M.K. Tseng, and A. Atrens, Stress Corrosion Cracking and Hydrogen Embrittlement of an Al-Zn-Mg-Cu Alloy, *Acta Mater.*, 2004, **52**, p 4727–4743
14. R.K. Viswanadham, T.S. Sun, and J.A.S. Green, Grain Boundary Segregation in Al-Zn-Mg Alloys—Implications to Stress Corrosion Cracking, *Metall. Mater. Trans. A*, 1980, **11**, p 85–89
15. K. Kyzioł, K. Koper, M. Środa, M. Klich, and Ł. Kaczmarek, Influence of Gas Mixture During N + Ion Modification Under Plasma Conditions on Surface Structure and Mechanical Properties of Al-Zn Alloys, *Surf. Coat. Technol.*, 2015, **278**, p 30–37
16. C.M. Abreu, M.J. Cristóbal, R. Figueroa, and G. Pena, Wear and Corrosion Performance of Two Different Tempers (T6 and T73) of AA7075 Aluminium Alloy After Nitrogen Implantation, *Appl. Surf. Sci.*, 2015, **327**, p 51–61
17. Ł. Kaczmarek, M. Steglinski, J. Sawicki, J. Swiniarski, D. Batory, K. Kyzioł, Ł. Kołodziejczyk, W. Szymanski, P. Zawadzki, and D. Kottfer, Optimization of the Heat Treatment and Tribological Properties of 2024 and 7075 Aluminium Alloys, *Arch. Metall. Mater.*, 2013, **58**, p 535–540
18. K.D. Ralston, D. Fabijanic, and N. Birbilis, Effect of Grain Size on Corrosion of High Purity Aluminium, *Electrochim. Acta*, 2011, **56**, p 1729–1736
19. K.D. Ralston, N. Birbilis, and C.H.J. Davies, Revealing the Relationship Between Grain Size and Corrosion Rate of Metals, *Scr. Mater.*, 2010, **63**, p 1201–1204
20. M. Chen, Y. Deng, J. Tang, S. Fan, and X. Zhang, A Study of the Crystallographic Pitting Behavior of Al-0.54Mg-0.66Si Aluminum Alloy in Acidic Chloride Solutions, *Mater. Charact.*, 2019, **148**, p 259–265
21. C. Meng, D. Zhang, L. Zhuang, and J. Zhang, Correlations Between Stress Corrosion Cracking, Grain Boundary Precipitates and Zn Content of Al-Mg-Zn Alloys, *J. Alloys Compd.*, 2016, **655**, p 178–187
22. V.S. Sinyavskii, V.V. Ulanova, and V.D. Kalinin, On the Mechanism of Intergranular Corrosion of Aluminum Alloys, *Prot. Metals*, 2004, **40**, p 481–490
23. H.C. Fang, H. Chao, and K.H. Chen, Effect of Recrystallization on Intergranular Fracture and Corrosion of Al-Zn-Mg-Cu-Zr Alloy, *J. Alloys Compd.*, 2015, **622**, p 166–173
24. X. Lu, X. Han, Z. Du, G. Wang, L. Lu, J. Lei, and T. Zhou, Effect of Microstructure on Exfoliation Corrosion Resistance in an Al-Zn-Mg Alloy, *Mater. Charact.*, 2018, **135**, p 167–174
25. G. Peng, K. Chen, H. Fang, and S. Chen, Effect of Cr and Yb Additions on Microstructure and Properties of Low Copper Al-Zn-Mg-Cu-Zr Alloy, *Mater. Des.*, 2012, **36**, p 279–283
26. S. Chen, K. Chen, P. Dong, S. Ye, and L. Huang, Effect of Recrystallization and Heat Treatment on Strength and SCC of an Al-Zn-Mg-Cu Alloy, *J. Alloys Compd.*, 2013, **581**, p 705–709
27. Y. Shi, Q. Pan, M. Li, X. Huang, and B. Li, Effect of Sc and Zr Additions on Corrosion Behaviour of Al-Zn-Mg-Cu Alloys, *J. Alloys Compd.*, 2014, **612**, p 42–50
28. H.C. Fang, H. Chao, and K.H. Chen, Effect of Zr, Er and Cr Additions on Microstructures and Properties of Al-Zn-Mg-Cu Alloys, *Mater. Sci. Eng. A*, 2014, **610**, p 10–16
29. J.F. Li, N. Birbilis, C.X. Li, Z.Q. Jia, B. Cai, and Z.Q. Zheng, Influence of Retrogression Temperature and Time on the Mechanical Properties and Exfoliation Corrosion Behavior of Aluminium Alloy AA7150, *Mater. Charact.*, 2009, **60**, p 1334–1341
30. S.P. Knight, K. Pohl, N.J.H. Holroyd, N. Birbilis, P.A. Rometsch, B.C. Muddle, R. Goswami, and S.P. Lynch, Some Effects of Alloy Composition on Stress Corrosion Cracking in Al-Zn-Mg-Cu Alloys, *Corros. Sci.*, 2015, **98**, p 50–62
31. A.C.U. Rao, V. Vasu, M. Govindaraju, and K.V.S. Srinadh, Stress Corrosion Cracking Behaviour of 7xxx Aluminium Alloys: A Literature Review, *Trans. Nonferr. Metals Soc.*, 2016, **26**, p 1447–1471
32. G.M. Scamans, Discontinuous Propagation of Stress Corrosion Cracks in Al-Zn-Mg Alloys, *Scr. Metall.*, 1979, **13**, p 245–250
33. L. Christodoulou and H.M. Flower, Hydrogen Embrittlement and Trapping in Al-6%Zn-3%Mg, *Acta Metall.*, 1980, **28**, p 481–487
34. D. Hardie, N.J.H. Holroyd, and R.N. Parkins, Reduced Ductility of High-Strength Aluminium Alloy During or After Exposure to Water, *Metal Sci.*, 1979, **13**, p 603–610
35. E. Dix, Acceleration of the Rate of Corrosion by High Constant Stresses, *AIME Trans*, 1940, **137**, p 11–40
36. Y. Shi, Q. Pan, M. Li, X. Huang, and B. Li, Influence of Alloyed Sc and Zr, and Heat Treatment on Microstructures and Stress Corrosion Cracking of Al-Zn-Mg-Cu Alloys, *Mater. Sci. Eng. A*, 2015, **621**, p 173–181
37. D. Tanguy, B. Bayle, R. Dif, and T. Magnin, Hydrogen Effects During IGSCC of pure Al-5Mg Alloy in NaCl Media, *Corros. Sci.*, 2002, **44**, p 1163–1175
38. D. Najjar, T. Magnin, and T.J. Warner, Influence of Critical Surface Defects and Localized Competition Between Anodic Dissolution and Hydrogen Effects During Stress Corrosion Cracking of a 7050 Aluminium Alloy, *Mater. Sci. Eng. A*, 1997, **238**, p 293–302

Publisher's Note Springer Nature remains neutral with regard to jurisdictional claims in published maps and institutional affiliations.